Theoretical and experimental approaches for the determination of functional properties of MgSnN2 thin films

Fahad Alnjiman, Agathe Virfeu, David Pilloud, Sébastien Diliberto, Emile Haye, Alaa Giba, Sylvie Migot, Jaafar Ghanbaja, Pascal Boulet, Hamad Albrithen, et al.

Version of Record: https://www.sciencedirect.com/science/article/pii/S0927024822002173
Manuscript_ea0dcbd5137f5c446b57328c9c04bdcd

Theoretical and experimental approaches for the determination of functional properties of $MgSnN_2$ thin films

Fahad Alnjiman[a,b,±], Agathe Virfeu[a,±], David Pilloud[a], Sébastien Diliberto[a], Emile Haye[c,d], Alaa E. Giba[a,e], Sylvie Migot[a], Jaafar Ghanbaja[a], Pascal Boulet[a], Hamad Albrithen[b,f], Jean-François Pierson[a, *]

[a] Institut Jean Lamour (UMR CNRS 7198), Université de Lorraine, Nancy, France

[b] Research Chair for Tribology, Surface, and Interface Sciences, Department of Physics and Astronomy, College of Science, King Abdullah Institute for Nanotechnology, King Saud University, Riyadh 11451, Saudi Arabia

[c] Laboratoire Interdisciplinaire de Spectroscopie Electronique (LISE), University of Namur, 5000 Namur, Belgium

[d] Laboratoire d'Analyse par Réactions Nucléaires (LARN), University of Namur, 5000 Namur, Belgium

[e] National Institute of Laser Enhanced Sciences, Cairo University, Giza 12613, Egypt

[f] King Abdullah City for Atomic and Renewable Energy (K.A.CARE), Energy Research and Innovation Center, Riyadh, Saudi Arabia

* corresponding author: jean-francois.pierson@univ-lorraine.fr

[±] These authors equally contributed to the present work

Abstract

$MgSnN_2$ thin films were deposited by reactive magnetron co-sputtering on fused silica and silicon substrates. The properties of the films were determined as a function of the deposition temperature. Although the films exhibited a strong preferred orientation along the [002] direction, cumulative X-ray diffractograms at various χ angles evidenced that the deposited films crystallized in a wurtzite-like structure. Regardless of the substrate temperature during deposition, $MgSnN_2$ films had a columnar microstructure. Mössbauer spectrometry and X-ray photoemission spectroscopy were used to extract the chemical environment of magnesium and tin atoms and to identify their oxidation states. Electrical properties were deduced from Hall effect measurements. An increase of the electron mobility was noticed at high deposition temperature. The optical band gap of $MgSnN_2$ films increased from approx. 2.28 to 2.43 eV in the 300 – 500 °C range. The experimental optical properties of $MgSnN_2$ films were compared to those obtained by *ab initio* calculations.

Keywords: $MgSnN_2$; Reactive co-sputtering ; optical and electrical properties ; *ab initio* calculations ; Burstein Moss effect

1. Introduction

III-N materials are commonly used in several applications such as visible and UV LEDs, fast high power transistors, solar cells and mechanical devices[1,2]. The main spinneret is based on the use of InGaN alloys. However, such materials contain indium and gallium. Significant volatility in their price and demand over the last years has led to considerable concern given their critical roles and their use in a wide range of large-scale electronic devices[3,4]. Moreover, at present the crystalline III-N materials require the use of epitaxial growth techniques with high cost and relative complexity. Thus, it is important to study and develop new earth abundant materials with optimized properties for the processing of innovative optoelectronic devices that can be competitivelymore cost effectiveand sustainable for mass production.

Following the inorganic thin film strategy where the III-N materials have already been proven to be very stable, it is so natural to focus on inadequately investigated semiconductor materials that are closely related to the III-N family. In such new compounds, the elements of the column IIIare replaced by an ordered cation sublattice composed of equal numbers of elements of column II (Mg, Zn) and column IV (Si, Ge, Sn) atoms.Such a strategy has been successfully used to develop $ZnSnN_2$ and $ZnGeN_2$ or $Zn(Sn,Ge)N_2$[5–18].

Few theoretical studies have been reported for $MgSnN_2$[19–22]. $MgSnN_2$ thin films have already been grown by plasma assisted molecular beam epitaxy (PAMBE)[23], radiofrequency (RF) sputtering[24,25], or by using a high-pressure-metathesis reaction[26]. As for $ZnSnN_2$ one of the mainchallenge in the study of $MgSnN_2$ is the precise determination of its structure. By using the quasiparticle-self-consistent GW approximation,Jaroenjittichai*et al.*[22]have proposed aβ-$NaFeO_2$-like structure (spacegroup $Pna2_1$) for $MgSnN_2$. However, in their report the authorshave mentionned that the band gap of $MgSnN_2$ is close to theone of GaN, i.e. 3.4 eV.In the work ofRasander*et al.*[21]structural and elastic properties have been calculated for the orthorhombic $Pna2_1$ $MgSnN_2$ structure. However,a disorderedwurtzite-like structure with overall orthorhombic symmetry was also proposed for the Zn-IV-N_2 family[27]. By using the metathesis reaction under high pressure,Kawamura *et al.*[26] have synthesized $MgSnN_2$ with a disordered rocksalt-like structure.Greenaway*et al.*[24]have suggested several possible structures for $MgSnN_2$ thin films,they also mention that the cation ordering may change the structure. Yamada *et al.*[25]have epitaxially grown $MgSnN_2$ on GaN(001),indicating an hexagonal ZnO-like structure for their films.Since several structures

have been reported for $MgSnN_2$ films, their properties vary within a large range. For example, the optical band gap of $MgSnN_2$ films vary in the 1.8- 3.4 eV range[20–26]. This variation of the band gap canmainly be attributedto the cation ordering in the structure.

In the present work, $MgSnN_2$ films have been deposited on fused silica and silicon substrates by reactive magnetron co-sputtering. While maintaining Mg/Sn atomic ratio constant, the deposition temperature has been changed for the different films. The structural, microstructural, optical and electrical properties of the grown films have been investigated. In addition, the electronic and optical properties were calculated by density functional theory (DFT) with an accurate hybrid functional (mBJ) to predict band gap energy.The results obtained in the present study are helpful to determine the potential applications of $MgSnN_2$ thin films for solar applications.

2. Experimental details

2.1. Thin film deposition and characterization

$MgSnN_2$ thin films were deposited by reactive magnetron co-sputtering at different substrate temperatures (T_{sub}) (up to 500°C) using two metallic targets (Mg and Sn) in a pure nitrogen atmosphere. The target diameter was 50.8mm and the distance between the targets and the substrate holder was fixed to 90 mm. The substrate-holder was a rotating inconelmolyblock on which the substrates (fused silica and silicon substrates of 2×2 cm^2)were fixed and heated from 100 to 500°C.The self-established temperature at the substrate was measured using a thermocouple.Prior to their introduction into the chamber, the substrates were cleaned by ethanol. Before the film deposition, an etching step using a radiofrequency plasma (50 W, 5 min) wasperformed to clean the substrate surfaces. During the growth process,the total pressure was kept at 1 Pa with a nitrogen flow rate of 30 sccm. The targets were sputtered by fixing the RF power at190 W on the Mg target and the DC current at 0.25 Aon the Snone. The growth rate for $MgSnN_2$was approx. 3.0 μm/h. The deposition procedure used for the $MgSnN_2$film growth is highly reproducible. The atomic Mg / Sn ratio in the film wasdetermined using an energy dispersive spectrometer (EDS) coupled with a scanning electron microscope (ZEISS Gemini SEM 500 equipped with field emission gun). The quantification by EDS was done at 20kV. The film structure was characterized by θ–2θ X-ray diffraction (XRD) measurements with a Bruker D8 Advance diffractometer using a Cu anode (λ_{Cu} $K_{\alpha 1}$ =1.5406 Å). To obtain more information about the crystal structure of the deposited

films, a Brucker D8 Discover diffractometer (λ_{Co} $K_{\alpha 1,2}$ = 1.79026 Å) was also used for detexturation. The film microstructure was characterized by transmission electronic microscopy (TEM) using a JEOL – ARM 200 F Cold FEG TEM/STEM operating at 200 kV and equipped with a spherical aberration (Cs) probe corrector (point resolution 0.12 nm in TEM mode and 0.078 nm in STEM mode). The cross-section of the samples was prepared by using a focused ion beam (FIB) scanning electron microscope (SEM) dual beam system FEI Helios NanoLab 600i. The thickness of the films was measured by a Bruker DektakXT tactile profilometer in good agreement with those obtained from TEM cross-section observations. ^{119}Sn conversion electron Mössbauer spectrometry (CEMS) spectra were recorded by a conventional Mössbauer spectrometer (Wissel) with a flowing gas (96% He, 4% CH_4) proportional counter (Rikon-5) at room temperature. The velocity scale was calibrated with a ^{57}CoRh source and a metallic iron foil. The evaluation of Mössbauer spectra was performed by least square fitting of lines using the Winnormos (Wissel) program. The velocity error on all of the ^{119}Sn Mössbauer spectra was ±0.1mms^{-1}. X-ray photoelectron spectroscopy (XPS) was carried out to further investigate the chemistry of $MgSnN_2$ thin films. The analysis was done using a Thermo K-Alpha, working with Al Kα radiation (1486.68 eV), with a spot size of 250 x 250 µm². The high resolution spectra of Mg 1s, N 1s, O1s, Sn 3d, Mg KLL levels and valence band were recorded at a pass energy of 20eV, with 20 scans. The survey spectra were also recorded, and did not reveal contamination of the samples, except of carbon and oxygen. Prior to analysis, the surface was cleaned by Ar^+ etching. The etching was done under mild condition (200 eV, 60 s, medium current), to limit the chemistry alteration of the coating, while removing the contamination layer. Although such parameters limit film damage, a slight reduction was still possible. A flood gun is used during measurement to limit the charge shift. The spectra analysis was done by being aware of the C 1s reference problem and the charge effect of insulating samples [28–30]. The possible charge shift of each sample was analysed prior to analysis, then the spectra were calibrated with the same shift for each level, to obtained consistent results with the position of the valence band edge. The peak analysis was carried out using Thermo Avantage software, considering a Shirley background.The optical UV-visible-NIRtransmittance measurements were performed in the 200-2500 nm range using Varian Cary 7000 UV-vis-NIR spectrometer within a UMA configuration. Electrical properties were measured at room temperature using a Hall effect equipment (Ecopia HMS5000).The photoluminescence (PL) measurements were performed using a spectrofluorometer (Fluorolog-Horiba). A xenon arc lamp source (380 nm) was used,

and the PL emission was analysed with a detection system equipped with 150 grooves/mm gratings and a cooled silicon-based CCD camera.

2.2. First-principle calculations

Density functional theory (DFT) geometry relaxation were carried out using the plane-wave Vienna *ab initio* simulation package (VASP)[31,32].The generalized gradient approximation (GGA) in the PBE (Perdew-Burke-Ernzerhof) functional was selected for the exchange-correlation potential. The k-points 15x15x10Monkhorst-Pack were used for Brillouin zone integration with a Γ-centered k-point mesh. All lattice vectors and atomic positions were fully relaxed by minimization of the quantum mechanical stresses and forces using the projector-augmented wave (PAW) VASP pseudopotentials. The cut-off energy for plane-waves was set to 520 eV. Each atom was configurationally relaxed until the forces were under 0.02 eV/Å, and convergence in energy iterations of 10^{-7} eV/atom was used. Initially the structures were taken from the crystallographic information files (CIF) available from the previous work of Greenaway *et al.* [24].For the electronic band structures we used the full-potential linearized augmented plane wave (FLAPW) approach, as implemented in the WIEN2K code[33]. In this method, a plane-wave cutoff corresponding to $R_{MT}K_{max}$= 7 was chosen to avoid overlapping during the band structure calculation. The radial wave functions inside the non-overlapping muffin-tin spheres were expanded up to l_{max} = 12. The charge density was Fourier expanded up to G_{max} = 16 $Å^{-1}$. Total energy convergence was achieved with respect to the Brillouin zone (BZ) integration mesh with 500 k-points. Because GGA exchange-correlation functional are known to underestimate actual band gaps, we used the modified Becke-Johnson (mBJ) functional which leads to excellent agreement with the experimental values for the energy separation between valence band maximum (VBM) and conduction band minimum (CBM) [34]. We used 5000 k-points in the BZ to compute the band derivatives, the density of states and calculate optical properties such as absorption coefficient and refractive index.

3. Results and discussion

3.1. Structure and composition

Table 1 shows the chemical composition of $MgSnN_2$ thin films deposited at different substrate temperatures (T_{sub}). Since the EDS method used to determine the film composition may

overestimate the nitrogen content in the film due to the signal of nitrogen diffused in the substrate, the atomic ratio Mg/(Mg+Sn) is preferred to show the effect of the deposition temperature on the film composition. From the data provided in Table 1, it clearly appears that the metallic content is not influenced by the change of the substrate temperature. Moreover, both Mg and Sn are equally present in the film.

In Figure1, the XRD analysis in specular Bragg-Brentano configuration clearly shows theinfluence of the substrate temperature on $MgSnN_2$ thin films. The diffractograms only evidence the occurrence of the $MgSnN_2$ phase. No metallic phase such as Mg or Snis observed as reported in the previous work[24]. X-ray diffractogram of $MgSnN_2$can be indexed with the expected ZnO-likehexagonal structure(space group: $P6_3mc$) with the lattice parameters a=3.462 and c=5.504 Å. At room temperature, $MgSnN_2$thin film showsmainly3 diffraction peaks, namely (002), (102) and (103).The Figure 1 also evidences that the intensity of the(002) diffraction peak increases with substrate temperature,indicating a progressive improvement of the crystalline quality of the films with the deposition temperature. The emergence of the (004) peak is also observed from 300°C and its intensity rises up with the temperature. This can been explained by the increase of the adatom mobility[35]. Between 100 and 500°C, the films show a strong preferred orientation along the [002] direction. This fiber texture is usually observed for hexagonal structure like ZnO[36]and $ZnSnN_2$[37].

Based on the X-ray diffractograms, the coherence length (or crystallite size) has been estimated from the full width at half maximum (FWHM) of the (002) diffraction peak using the Scherrer equation. In Table 2,the FWHM and the coherence lengthvariations are shown versus the substrate temperature. By increasing the substrate temperature, the coherence length was found to increase. Once again, this result can be correlated with the increaseof the adatom mobility and also the thermally induced grain growth[35,38].

By using specularBragg-Brentano configuration analysis it was not possible to precisely determine the film structure due to the strong texture of films deposited at a temperature higher or equal to 100 °C. Figure 2 presents the cumulative X-ray diffractograms obtained at various χ angles of $MgSnN_2$ films on fused silica substrates with different temperatures, this method being already described byBouhtiyya*et al.*[39].Within this method, the highly textured $MgSnN_2$ films exhibit a powder-like diffractogram. All diffraction peaks match with the hexagonal structure and the$MgSnN_2$diffractogramscan be fitted with the ZnO-like structure (space group $P6_3mc$) with lattice parameters a=3.459 and c=5.507 Å, giving a c/aratio of 1.592 in close agreement with the ideal value known for such a structure.In the

literature, the crystal structure for $MgSnN_2$ is considered as wurtzite structure with overall orthorhombic symmetry with space group $Pna2_1$ which is known for β-$NaFeO_2$[40]. In the first synthesis of $MgSnN_2$ by MBE,the authors found that the films exhibit a wurtzite-derived structure[23]. By using the metathesis reaction under high pressure[26]the authors reported non-stoichiometric $MgSnN_2$films with a Mg/Sn atomic ratio of 1.19 crystallizing in a disordered rocksalt-like structure with lattice parameter a=4.48 Å. By using RF-sputtering[24] $MgSnN_2$ films were described as a cation-disordered wurtzite structure with group space $Pna2_1$.

The $MgSnN_2$ film microstructure has been characterized by TEM (Figure 3). Bright field images of the film cross section are presented in Figures 3a and 3d for films grown at room temperature and 500°C, respectively. For both films, a columnar microstructure is clearly evidenced as shown also in dark fieldimages (Figures 3b and 3e).Such a columnar microstructure is commonly observed for sputtered binary nitride coatings[41–43]and ternary nitride films[6,44]. The width of the columns for the sample grownat room temperature is varying between 37 and 52 nm(Fig. 3a) while the column width is ranging between 40 and 53 nm for the film grown atT_{sub}= 500°C (Fig. 3c). The selected area electron diffraction (SAED) pattern on several columns is shown in the insetsof figures 3a and 3d. These SAED patterns are in well agreement with those obtained by XRD. The electron diffraction pattern obtained on the film deposited at room temperature shows several rings characteristics of a polycrystalline material without preferred orientation. On the other hand,for the film grown at T_{sub}= 500°C the SAED patternindicates a preferred orientation along the [001] direction.High resolution image of one column is depicted in Figure 3c for T_{sub}= room temperature and Figure 3f for T_{sub}= 500°C. As shown in the insetsof both figures, a single crystal of $MgSnN_2$ is clearly evidenced by FFT.

Figure 4 shows a Mössbauer spectrum obtained on the film grown at T_{sub} =400°C. The results obtained with the other samples are similar. They all demonstrate a doublet with an isomeric shift (IS) close to 1.06 mm s^{-1}, characteristic of tin atomswith an oxidation state +IV. The doublet also presents an asymmetry due to the strong texture of the thin film illustrated by X-ray diffraction measurements. Table 3 shows the hyperfine parameters obtained as a function of the deposition temperature. The stability of the isomeric shift observed along the series can be interpreted as a stable chemical composition with the deposition temperature. On the other hand, the quadrupole splitting (QS) decreases with increasing temperature. Few information on the Mössbauer parameters of tin nitride is available from the literature. For example, Lima

et al.[44] studied Sn_xN_y tin nitride films deposited by sputtering and demonstrated the presence of Sn^{4+} with IS = 1.1 mm s^{-1} and QS = 0.67 mm s^{-1}. More recently, Baggetto*et al.*[45] have characterized Sn_3N_4 films and have shown that in this spinel structure, the characteristic absorptions represent a sum of Sn^{4+} ions located in octahedral and tetrahedral sites with QS = 0 mm s^{-1}.The QS parameter is directly linked to the symmetry of the crystallographic site. A QS value close to 0.94mm s^{-1} indicates that the Sn^{4+}atomsare in an asymmetric site, i.e. a tetrahedral site elongated in one direction. A slight decrease in this parameter is observed with the deposition temperature, which appears to be consistent with better crystallization of the nitride phaseas temperature increases.

Figure 5 presents the XPS analysis of the $MgSnN_2$ films. Interestingly, no significant difference is observed between the various samples. Mg 1s signal (Figure 5a) is composed of one contribution centred at 1303.9 eV, in accordance with nitride formation [46] as metallic and oxide contribution are centred at approx. 1303.2 and 1305.0 eV, respectively. The Sn 3d signal (Figure 5b) is composed of two doublet contribution due to Sn 3d 5/2 and Sn 3d 3/2, centred at 484.9 and 486.4 eV, respectively. The more intense contribution at 486.4 eV (representing 90% of the area) is attributed to Sn^{4+} contribution. The literature presents a Sn^{4+} contribution at 486.1eV in Sn_xN_y[47] andat 486.8eV in Sn nitride film [48] while Ansari *et al.* reported Sn^{4+} at 486.3eV. The XPS results are consistent with Mössbauer spectroscopy results. The slight contribution at 484.9 eV is possibly due to Sn^{2+}[46–48]that may come from the etching of the surface, as no Sn^{2+} is evidenced by Mössbauer. The Mg/Sn atomic ratio obtained by XPS is closed to 55/45, and the little deviation from that given by EDS is attributed to the surface etching performed prior to the XPS analysis which altered slightly the surface stoichiometry. The formation of the nitride compound is further confirmed by the N 1s signal (Figure 5c), exhibiting one single contribution at 396.7eV. In addition to Mg 1s, the Mg KLL Auger level (Figure 5d) has been recorded, as it is more sensitive for chemical analysis. The signal is composed of an intense peak at 303.4eV (i.e. kinetic energy of 1183.3 eV) attributed to nitride, and a shoulder at 305.5 eV (i.e. kinetic energy of 1181.2 eV) attributed to oxide, in excellent agreement with the XPS analysis of Bouvier *et al.* on nitride powder [46]. The XPS valence band (Figure 5e) presents a strong peak at 25.9eV, attributed to Sn 4d level (this contribution has been reported at 26.7eV in $ZnSnN_2$[49]). In the 0-20 eV range, three contributions are observed at approx. 4, 8.5 and 16eV. The observed peak at approx. 4eV can be attributed to the N-2p and Sn-5s in accordance with our DOS calculations.

However, the range of calculations does not allow to attribute the two others contributions.The valence band spectra presented in Fig. 5e has been obtained using XPS analyses. From these experiments, the valence band maximum has been estimated to 0.3 eV independently of the deposition temperature. Such a result disagrees with the optical band gap measurements presented in Figure 8.

3.2. Optical and electrical properties

The film transmittance in the UV–visible-NIR range is presented in Fig. 6. The thickness of all films is in the 700-800 nm range. The transmittance spectra present prominent interference fringes caused by the multiple reflections at the two interfaces of the air / $MgSnN_2$ / fused silica substrate system. In the visible range, there is no strong influence of the deposition temperature on the film transmittance. Such a result may be explained considering that the deposition temperature has a weak influence on the chemical composition, the structure and the microstructure. However, a blue shift of the absorption threshold is noticed when the deposition temperature increases. The second difference observed on these transmittance spectra is related to the behaviour in the NIR domain. The increase of the deposition temperature comes with a progressive decrease of the NIR transmittance. The blueshift of the absorption threshold and the decrease of the NIR transmittance are related to changes in the electronic structure that influence the electronic properties of the $MgSnN_2$ films.$MgSnN_2$ thin films have been characterized by photoluminescence (Figure S1). The PL response was very weak and a long acquisition duration was necessary to obtain a signal. The very weak PL signal can be explained by the delocalization of excitons upon light excitation. It can be observed that the films of lower resistivity (higher conductivity) exhibit lower PL intensity at least by 2.5 times than the sample of highest resistivity prepared at room temperature. This could imply to the contribution of the delocalized carriers in PL quenching. Since no PL experiment has been previously reported on $MgSnN_2$, it was not possible to assign the large PL band centred at approx. 460 nm.

Table 4 summarizes the values of the $MgSnN_2$optical bandgap (E_g) determined from the transmittance data using the Tauc method. $MgSnN_2$ being reported as a direct semiconductor, the E_g value determination is based on the plot of $(\alpha h\nu)^2$ versus $h\nu$ and by extrapolating the full line to the abscissa (α denotes the absorption coefficient and $h\nu$ the photon energy)[50].Till a deposition temperature of 300°C, the optical band gap does not evolve

significantly. This parameter is approx. fixed to 2.28 eV. Further increase of the deposition temperature induces an enlargement of the band gap to 2.43 eV. Lowband gap value, i.e. 2.27 eV, well agrees with the theoreticalone calculatedby S. Lyu*et al.*(2.28 eV)[20]. Kawamura *et al.*[26]obtained a band gap of approx. 2.3 eV. Using spectroscopicellipsometry, Greenaway *et al.*[24] obtained a band gap close to 2.0 eV. Recently, Yamada *et al.*[25]have shown that $MgSnN_2$ thin film exhibits a band gap close to 2.3 eV.

The electrical resistivity and the mobility of $MgSnN_2$ thin films grown at different T_{sub} have been measured using Hall effect measurements (Figure 7).Whatever the deposition temperatures,$MgSnN_2$films exhibit a n-type behaviour. The electrical resistivity at room temperature tends to decrease as a function of the temperature. Within the T_{sub} range, the electrical resistivity drops from 0.137 (room temperature) to 0.012 Ωcm(500°C) although the band gap increases.This result can be correlated to the increaseof the coherence lengthas reported by X-ray diffraction(Table 2) and to the decrease of the amount of grains boundaries in the films deposited at high temperature. Duan*etal.* havealso reported the same behaviour by annealing $Bi_2Te_{2.7}Se_{0.3}$ thin films[51]. As well, the mobility vs. the substrate temperature is presented in Figure7. Compared to the electrical resistivity, the electron mobility increases with the temperature. Such behaviour was already reported in the literature in indium tin oxide thin films [52] or in nanocrystalline silicon [53]. These results support our explanation consideringthat the grain size influencesthe electrical resistivity as previously mentioned. The electron concentration of $MgSnN_2$ thin films was also determined by Hall effect measurements. Thecharge carrierconcentration varies from 1.8 to $2.9x10^{20}cm^{-3}$when T_{sub} increases from room temperature to 500°C (Figure 8).Such high values of charge carrier concentration suggest that $MgSnN_2$ thin films may be used as transparent conductive layers in optoelectronic devices. The first study of the electron concentration in $MgSnN_2$ is given by Greenaway *et al.*[24]for films grown by RF sputtering. They obtained an electron concentration in the 10^{19} - 10^{20} cm^{-3}range. Yamada *et al.*[25] have measured the electron concentration of $MgSnN_2$ for various Mg and Sn contents. They obtained an electron concentration in the 10^{18} cm^{-3} range for the Mg rich film and 10^{20} $cm^{-3}$for Sn rich ones. The evolution of the optical band gap as a function of the deposition temperature is also reported in Figure 8. Interestingly, a correlation is obtained on the charge carrier density and the optical band gap evolution as a function of the temperature. The increase of the optical band gap could be explained and interpreted using the Burstein–Moss effect (ΔE_g^{BM})due to carrier

concentration (n_e) in the film. In n-type semiconductors, the optical band gap (E_g^{opt}) can be expressed as[9]:

$$E_g^{opt} = E_g^{int} + \Delta E_g^{BM} = E_g + \frac{\hbar^2}{2m_{vc}^*}(3\pi^2 n_e)^{\frac{2}{3}} \quad (1)$$

Where E_g^{int} is the intrinsic bandgap energy and m_{vc}^* is s the reduced effective mass and is derived from the valence and conduction band effective masses, $m_v^*$and m_c^*, according to $\frac{1}{m_{vc}^*} = \frac{1}{m_v^*} + \frac{1}{m_c^*}$. However, theBurstein-Moss effect has been reported for $MgSnN_2$thin films with a charge carrier concentration higher than 10^{20} cm^{-3} [25].The Burstein-Moss effect is also mentioned in similar ternary nitride $ZnSnN_2$[9,54–57].

In the present work, an experimental reduced effective mass (m_{vc}^*) has been calculated by using the data from figure 8. Using the term $\Delta E_g^{BM}$from the equation (1),the reduced effective mass was calculated.In figure 9 the optical band gap was plottedvs. the carrier density over the power $^2/_3$. The slope was calculated by fitting these points linearly and was found to be 1.09 $x10^{-14}$ $eVcm^2$, leading to$m_{vc}^* = 0.3m_e$. This value is the first experimental result for hexagonal $MgSnN_2$have the same stoichiometrywhileYamada *et al.* [25] have reported that calculated $m_{vc}^*$is expected to be $\sim 0.7m_e$for hexagonal $MgSnN_2$withvarious stoichiometries.

3.3. Computed electronic and optical properties

In some previous work, Dumre*et al.* havecalculated the formation energies of the three different structures: disordered rocksalt, disordered wurtzite and orthorhombic[19]. The orthorhombic phase is more stable than the other structures of $MgSnN_2$. One year before, Greenaway *et al*. also showed that the $Pna2_1$ and $Pmc2_1$ (called wurtzite-type) are the most energetically favourable[24]. Although the XRD and TEM characterisations converged to a wurtzite ZnO structure, it remains complicated to create a cation-disordered wurtzite-derived crystal structure with the space group $P6_3mc$ due to the same positions of random substituted Mg and Sn atoms. For all these reasons, the two orthorhombic unit-cells with $Pna2_1$ and $Pmc2_1$ structures were investigated in the present study. The calculations have been solved with a number of point k = 5000 within the Brillouin zone and performed with the Wien2K code. The mBJ functional is based on the optimized effective potential method (OEP). This correction is as accurate as hybrid functionals for band gap prediction with a lower cost[58]. The band structure and the corresponding density of states for the two structures are plotted in Figure 10. These electronic calculations confirm the direct band gap of both orthorhombic

$MgSnN_2$ with valence band maximum (VBM) and conduction band minimum (CBM) located at the Γ point of the Brillouin zone. The direct band gaps for the $Pna2_1$ and the $Pmc2_1$ structures areE_G = 2.34 and 2.23 eV,respectively. Thus, the experimental optical band gap energy that varies from 2.28 to 2.43 eV (Table 4) are in good agreement with the predicted ones.

The projected density of states (PDOS) of $MgSnN_2$ for the two orthorhombic structures are represented in Figure 11. We can deduce that the top of the valence band maximum mainly results from the N-2p contribution with Mg 2pand Sn 5p and 4d states, while the minimum of the conduction band is dominated by N 2s and 2p with Sn 5s orbitals, leading to sp^3-hybridization in tetrahedral coordination. The largest contribution to Sn 5s states is comparable for both space groups $Pna2_1$ and $Pmc2_1$ in the lower-energy of the valence band (below -4 eV) and in the CBM. The two structures exhibits quite similar hybridization between N-2p and metallic atoms (mostly p states) in the VBM, which implies the presence of p-p coupling state.

In a previous work, Punya *et al*. calculated a larger band gap energy but a PDOS with the same contribution of atoms orbitals[22]. Moreover, by the determination of *x*, *y*, *z* effective masses for VBM and CBM state, they explained that the low dispersion of the lowest conduction band is due to the small electron effective mass.

Figure 12a compares the absorption coefficient calculated from UV-vis transmittance spectra and computed absorption coefficient for the two structures $Pna2_1$ and $Pmc2_1$. The interference fringes correspond to multiple reflections by the different surfaces. The small difference in the absorption threshold between the $Pna2_1$ and $Pmc2_1$ is the due to the small deviation in band gap energy. The best agreement between theoretical and experimental absorption coefficient is observed for 400°C and 500°C. All the films exhibit coefficient absorption more than $10^4 cm^{-1}$ which means that they could be good candidates for optical applications like LEDs active layers.The refractive index and extinction coefficient are also predicted from optoelectronic calculations and have been presented in Figure 12b. The same behaviour is observed for the two space groups with a constant offset for both. In the 0 – 4 eV energy range, the simulated refractive indexes vary from approx. 2.1 to 2.35 and from 2.0 to 2.1 for the two structures $Pna2_1$ and $Pmc2_1$, respectively. The extinction coefficient started to rise from the band gap energy to about 0.4 and 0.25 for the two space group $Pna2_1$ and $Pmc2_1$. These values are comparable with the optical properties measured and calculated from

spectroscopic ellipsometry[24]. The refractive index at different temperatures were given between 1.9 and 2.3 and the extinction coefficient goes up to 0.2 and 0.5 at 4 eV.

6. Conclusion

Using a reactive co-sputtering process, $MgSnN_2$ thin films have been deposited on fused silica and silicon substrates at different temperatures. The XRD results showsno metallic phases of Mg or Sn andthat all samples crystallize in the hexagonal structure. At room temperature $MgSnN_2$ thin film show a random orientation in [002], [102] and [103] directions, while a strong preferred orientation along the [001] direction is noticed as soon as the deposition temperature is 100°C. The intensity of the (002) diffraction peak increases with substrate temperature, indicating a progressive improvement of the film crystalline quality.Based on TEM cross section observations, $MgSnN_2$ films grow with a columnar microstructure. Mössbauer spectrometry have been used to characterize the chemical environment of tin atoms. Only Sn^{4+} atoms in tetrahedral configuration have been evidenced by Mössbauer. Such a result has been also confirmed by XPS analyses. Using Hall effect measurements,the electrical resistivity and the mobility of $MgSnN_2$ thin films grown with different T_{sub} have been measured.As a function of the temperature, charge carrier concentration and mobility exhibit opposite behaviour. The electron mobility is ranging between0.25 and 1.67 $cm^2V^{-1}s^{-1}$while the electrical resistivity drops from 0.137 to 0.012 Ωcm. Furthermore, the optical band gap of $MgSnN_2$ thin films could be tuned from 2.27 to 2.43 eV by increasing T_{sub}. However, Burstein-Moss effect has been deduced from optical and electrical measurements.Finally,an experimental reduced effective mass (m^*_{vc}) was calculated to be $m^*_{vc} = 0.3m_e$. The DFT calculations show that the optoelectronic properties of the two most stable phases of $MgSnN_2$ are in good agreement with the films characterised at different temperature. The electronic band gap energy ispredicted at 2.34 eV and 2.23 eV for orthorhombic $Pna2_1$ and $Pmc2_1$, respectively.Theoretical values of refraction index and extinction coefficient were calculated according to the photon energy and are close to the measured values reported.Due to the electrical and optical properties of these films, $MgSnN_2$ cannot be considered for application as light absorbing layer in single junction solar cells. Nevertheless, applications as transparent conductive layer in optoelectronic devices could be considered. Finally, the prepared $MgSnN_2$ films have the potential to be used as a large-bandgap light absorbing layer of multi-junction solar cells due to the high conductivity and moderate light absorption ability.

Acknowledgments

This work has been funded by the ANR-17-CE05-0022 OPERA project and the Contrat de Plan Etat-RégionMatDS. High Performance Computing resources were provided by the EXPLOR centre hosted by the Université de Lorraine. The Centres de CompétencesDaυmand Optique Laser of the Institut Jean Lamour are acknowledged for the access to their equipment. The authors would like to thank Prof. E. Gaudry of the Institut Jean Lamour for her computational skills and useful advices.

Data availability

The raw/processed data required to reproduce these findings cannot be shared at this time as the data also forms part of an ongoing study.

[1] S. Nakamura, M. Senoh, S. Nagahama, N. Iwasa, T. Yamada, T. Matsushita, H. Kiyoku, Y. Sugimoto, T. Kozaki, H. Umemoto, M. Sano, K. Chocho, InGaN/GaN/AlGaN-based laser diodes with modulation-doped strained-layer superlattices grown on an epitaxially laterally overgrown GaN substrate, Appl. Phys. Lett. 72 (1998) 211–213. https://doi.org/10.1063/1.120688.
[2] H. Amano, N. Sawaki, I. Akasaki, Y. Toyoda, Metalorganic vapor phase epitaxial growth of a high quality GaN film using an AlN buffer layer, Appl. Phys. Lett. 48 (1986) 353–355. https://doi.org/10.1063/1.96549.
[3] P. Ferro, F. Bonollo, Materials selection in a critical raw materials perspective, Mater. Des. 177 (2019) 107848. https://doi.org/10.1016/j.matdes.2019.107848.
[4] C.C. Pavel, A. Marmier, E. Tzimas, T. Schleicher, D. Schueler, M. Buchert, D. Blagoeva, Critical raw materials in lighting applications: Substitution opportunities and implication on their demand, Phys. Status Solidi -Appl. Mater. Sci. 213 (2016) 2937–2946. https://doi.org/10.1002/pssa.201600594.
[5] K. Javaid, W. Wu, J. Wang, J. Fang, H. Zhang, J. Gao, F. Zhuge, L. Liang, H. Cao, Band Offset Engineering in ZnSnN2-Based Heterojunction for Low-Cost Solar Cells, ACS Photonics. 5 (2018) 2094–2099. https://doi.org/10.1021/acsphotonics.8b00427.
[6] N. Beddelem, S. Bruyère, F. Cleymand, S. Diliberto, C. Longeaud, S. le Gall, R. Templier, P. Miska, B. Hyot, Structural and functional properties of Zn(Ge,Sn)N2 thin films deposited by reactive sputtering, Thin Solid Films. 709 (2020) 138192. https://doi.org/10.1016/j.tsf.2020.138192.
[7] K. Kumar Chinnakutti, V. Panneerselvam, S. Thankaraj Salammal, Ba-acceptor doping in ZnSnN2 by reactive RF magnetron sputtering: (002) faceted Ba–ZnSnN2 films, J. Alloys Compd. 855 (2021) 157380. https://doi.org/10.1016/j.jallcom.2020.157380.
[8] P.C. Quayle, E.W. Blanton, A. Punya, G.T. Junno, K. He, L. Han, H. Zhao, J. Shan, W.R.L. Lambrecht, K. Kash, Charge-neutral disorder and polytypes in heterovalent wurtzite-based ternary semiconductors: The importance of the octet rule, Phys. Rev. B. 91 (2015) 205207. https://doi.org/10.1103/PhysRevB.91.205207.
[9] X. Cao, F. Kawamura, Y. Ninomiya, T. Taniguchi, N. Yamada, Conduction-band effective mass and bandgap of ZnSnN 2 earth-abundant solar absorber, Sci. Rep. 7 (2017) 14987. https://doi.org/10.1038/s41598-017-14850-7.
[10] D.D. Le, T.S. Ngo, J.-H. Song, S.-K. Hong, Epitaxial Growth of Bandgap Tunable ZnSnN2 Films on (0001) Al2O3 Substrates by Using a ZnO Buffer, Cryst. Growth Des. 18 (2018) 1385–1393. https://doi.org/10.1021/acs.cgd.7b01285.
[11] A. Punya, W.R.L. Lambrecht, M. van Schilfgaarde, Quasiparticle band structure of Zn-IV-N2 compounds, Phys. Rev. B. 84 (2011) 165204. https://doi.org/10.1103/PhysRevB.84.165204.
[12] A.M. Shing, N.C. Coronel, N.S. Lewis, H.A. Atwater, Semiconducting ZnSnxGe1-xN2 alloys prepared by reactive radio-frequency sputtering, APL Mater. 3 (2015) 076104. https://doi.org/10.1063/1.4927009.
[13] Y. Wang, T. Ohsawa, X. Meng, F. Alnjiman, J.-F. Pierson, N. Ohashi, Suppressing the carrier concentration of zinc tin nitride thin films by excess zinc content and low temperature growth, Appl. Phys. Lett. 115 (2019) 232104. https://doi.org/10.1063/1.5129879.
[14] A.D. Martinez, A.N. Fioretti, E.S. Toberer, A.C. Tamboli, Synthesis, structure, and optoelectronic properties of II–IV–V2 materials, J. Mater. Chem. A. 5 (2017) 11418–11435. https://doi.org/10.1039/C7TA00406K.
[15] N. Feldberg, B. Keen, J.D. Aldous, D.O. Scanlon, P.A. Stampe, R.J. Kennedy, R.J. Reeves, T.D. Veal, S.M. Durbin, ZnSnN2: A new earth-abundant element semiconductor for solar cells, in: 2012 38th IEEE Photovolt. Spec. Conf. PVSC, 2012: pp. 002524–002527. https://doi.org/10.1109/PVSC.2012.6318108.
[16] P.C. Quayle, G.T. Junno, K. He, E.W. Blanton, J. Shan, K. Kash, Vapor–liquid–solid synthesis of ZnSnN2, Phys. Status Solidi B. 254 (2017). https://doi.org/10.1002/pssb.201600718.
[17] F. Deng, H. Cao, L. Liang, J. Li, J. Gao, H. Zhang, R. Qin, C. Liu, Determination of the basic optical parameters of ZnSnN2, Opt. Lett. 40 (2015) 1282–1285. https://doi.org/10.1364/OL.40.001282.

[18] A.N. Fioretti, E.S. Toberer, A. Zakutayev, A.C. Tamboli, Effects of low temperature annealing on the transport properties of zinc tin nitride, in: 2015 IEEE 42nd Photovolt. Spec. Conf. PVSC, 2015: pp. 1–5. https://doi.org/10.1109/PVSC.2015.7355694.
[19] B.B. Dumre, D. Gall, S.V. Khare, Stability, and electronic and optical properties of ternary nitride phases of MgSnN2: A first-principles study, J. Phys. Chem. Solids. (2021) 110011. https://doi.org/10.1016/j.jpcs.2021.110011.
[20] S. Lyu, W.R.L. Lambrecht, Quasiparticle self-consistent GW band structures of Mg-IV-N2 compounds: The role of semicore d states, Solid State Commun. 299 (2019) 113664. https://doi.org/10.1016/j.ssc.2019.113664.
[21] M.R. asander, M.A. Moram, Elastic constants of the II–IV nitride semiconductors MgSiN2, MgGeN2and MgSnN2, J. Phys. D : Appl. Phys. 51 (2018) 375101. https://doi.org/10.1088/1361-6463/aad41f.
[22] A.P. Jaroenjittichai, W.R.L. Lambrecht, Electronic band structure of Mg-IV-N2 compounds in the quasiparticle-self-consistent GW approximation, Phys. Rev. B. 94 (2016) 125201. https://doi.org/10.1103/PhysRevB.94.125201.
[23] R.A. Makin, K. York, S.M. Durbin, N. Senabulya, J. Mathis, R. Clarke, N. Feldberg, P. Miska, C.M. Jones, Z. Deng, L. Williams, E. Kioupakis, R.J. Reeves, Alloy-Free Band Gap Tuning across the Visible Spectrum, Phys. Rev. Lett. 122 (2019) 256403. https://doi.org/10.1103/PhysRevLett.122.256403.
[24] A.L. Greenaway, A.L. Loutris, K.N. Heinselman, C.L. Melamed, R.R. Schnepf, M.B. Tellekamp, R. Woods-Robinson, R. Sherbondy, D. Bardgett, S. Bauers, A. Zakutayev, S.T. Christensen, S. Lany, A.C. Tamboli, Combinatorial Synthesis of Magnesium Tin Nitride Semiconductors, J. Am. Chem. Soc. 142 (2020) 8421–8430. https://doi.org/10.1021/jacs.0c02092.
[25] N. Yamada, K. Matsuura, M. Imura, H. Murata, F. Kawamura, Composition-Dependent Properties of Wurtzite-Type Mg1+xSn1–xN2 Epitaxially Grown on GaN(001) Templates, ACS Appl. Electron. Mater. (2021). https://doi.org/10.1021/acsaelm.0c01115.
[26] F. Kawamura, M. Imura, H. Murata, N. Yamada, T. Taniguchi, Synthesis of a Novel Rocksalt-Type Ternary Nitride Semiconductor MgSnN2 Using the Metathesis Reaction under High Pressure, Eur. J. Inorg. Chem. 2020 (2020) 446–451. https://doi.org/10.1002/ejic.201901059.
[27] T.R. Paudel, W.R.L. Lambrecht, First-principles study of phonons and related ground-state properties and spectra in Zn-IV-N2 compounds, Phys. Rev. B. 78 (2008) 115204. https://doi.org/10.1103/PhysRevB.78.115204.
[28] G. Greczynski, L. Hultman, Compromising Science by Ignorant Instrument Calibration—Need to Revisit Half a Century of Published XPS Data, Angew. Chem. Int. Ed. 59 (2020) 5002–5006. https://doi.org/10.1002/anie.201916000.
[29] G. Greczynski, L. Hultman, X-ray photoelectron spectroscopy: Towards reliable binding energy referencing, Prog. Mater. Sci. 107 (2020) 100591. https://doi.org/10.1016/j.pmatsci.2019.100591.
[30] M.R. Linford, V.S. Smentkowski, J.T. Grant, C.R. Brundle, P.M.A. Sherwood, M.C. Biesinger, J. Terry, K. Artyushkova, A. Herrera-Gómez, S. Tougaard, W. Skinner, J.-J. Pireaux, C.F. McConville, C.D. Easton, T.R. Gengenbach, G.H. Major, P. Dietrich, A. Thissen, M. Engelhard, C.J. Powell, K.J. Gaskell, D.R. Baer, Proliferation of Faulty Materials Data Analysis in the Literature, Microsc. Microanal. Off. J. Microsc. Soc. Am. Microbeam Anal. Soc. Microsc. Soc. Can. 26 (2020) 1–2. https://doi.org/10.1017/S1431927619015332.
[31] G. Kresse, J. Furthmüller, Efficiency of ab-initio total energy calculations for metals and semiconductors using a plane-wave basis set, Comput. Mater. Sci. 6 (1996) 15–50. https://doi.org/10.1016/0927-0256(96)00008-0.
[32] G. Kresse, J. Furthmüller, Efficient iterative schemes for *ab initio* total-energy calculations using a plane-wave basis set, Phys. Rev. B. 54 (1996) 11169–11186. https://doi.org/10.1103/PhysRevB.54.11169.
[33] Blaha, P., Schwarz, K., Madsen, G. K., Kvasnicka, D., & Luitz, J. Wien2k. An augmented plane wave + local orbitals program for calculating crystal properties (2001)

[34] F. Tran, P. Blaha, Accurate Band Gaps of Semiconductors and Insulators with a Semilocal Exchange-Correlation Potential, Phys. Rev. Lett. 102 (2009) 226401. https://doi.org/10.1103/PhysRevLett.102.226401.
[35] Sputter Deposition Processes, Handb. Depos. Technol. Films Coat. (2010) 253–296. https://doi.org/10.1016/B978-0-8155-2031-3.00005-3.
[36] W. Chamorro, D. Horwat, P. Pigeat, P. Miska, S. Migot, F. Soldera, P. Boulet, F. Mücklich, Near-room temperature single-domain epitaxy of reactively sputtered ZnO films, J. Phys. D : Appl. Phys. 46 (2013) 235107. https://doi.org/10.1088/0022-3727/46/23/235107.
[37] F. Alnjiman, S. Diliberto, J. Ghanbaja, E. Haye, S. Kassavetis, P. Patsalas, C. Gendarme, S. Bruyère, F. Cleymand, P. Miska, P. Boulet, J.F. Pierson, Chemical environment and functional properties of highly crystalline ZnSnN2 thin films deposited by reactive sputtering at room temperature, Sol. Energy Mater. Sol. Cells. 182 (2018) 30–36. https://doi.org/10.1016/j.solmat.2018.02.037.
[38] J. Moravec, I. Novakova, J. Sobotka, H. Neumann, Determination of Grain Growth Kinetics and Assessment of Welding Effect on Properties of S700MC Steel in the HAZ of Welded Joints, Metals. 9 (2019) 707. https://doi.org/10.3390/met9060707.
[39] S. Bouhtiyya, R. Lucio Porto, B. Laïk, P. Boulet, F. Capon, J.P. Pereira-Ramos, T. Brousse, J.F. Pierson, Application of sputtered ruthenium nitride thin films as electrode material for energy-storage devices, Scr. Mater. 68 (2013) 659–662. https://doi.org/10.1016/j.scriptamat.2013.01.030.
[40] A.P. Jaroenjittichai, W.R.L. Lambrecht, Electronic band structure of Mg-IV-N2 compounds in the quasiparticle-self-consistent GW approximation, Phys. Rev. B. 94 (2016) 125201. https://doi.org/10.1103/PhysRevB.94.125201.
[41] L. Hultman, Thermal stability of nitride thin films, Vacuum. 57 (2000) 1–30. https://doi.org/10.1016/S0042-207X(00)00143-3.
[42] A.E. Giba, P. Pigeat, S. Bruyere, H. Rinnert, F. Soldera, F. Mücklich, R. Gago, D. Horwat, Strong Room Temperature Blue Emission from Rapid Thermal Annealed Cerium-Doped Aluminum (Oxy)Nitride Thin Films, ACS Photonics. 4 (2017) 1945–1953. https://doi.org/10.1021/acsphotonics.7b00233.
[43] A.E. Giba, P. Pigeat, S. Bruyère, T. Easwarakhanthan, F. Mücklich, D. Horwat, Controlling refractive index in AlN films by texture and crystallinity manipulation, Thin Solid Films. 636 (2017) 537–545. https://doi.org/10.1016/j.tsf.2017.06.057.
[44] R.S. Lima, P.H. Dionisio, W.H. Schreiner, C. Achete, Magnetron sputtered tin nitride, Solid State Commun. 79 (1991) 395–398. https://doi.org/10.1016/0038-1098(91)90491-D.
[45] L. Baggetto, N.A.M. Verhaegh, R.A.H. Niessen, F. Roozeboom, J.-C. Jumas, P.H.L. Notten, Tin Nitride Thin Films as Negative Electrode Material for Lithium-Ion Solid-State Batteries, J. Electrochem. Soc. 157 (2010) A340–A347. https://doi.org/10.1149/1.3290778.
[46] Y. Bouvier, B. Mutel, J. Grimblot, Use of an Auger parameter for characterizing the Mg chemical state in different materials, Surf. Coat. Technol. 180–181 (2004) 169–173. https://doi.org/10.1016/j.surfcoat.2003.10.062.
[47] D. Lützenkirchen-Hecht, R. Frahm, Structure of reactively sputter deposited tin-nitride thin films: A combined X-ray photoelectron spectroscopy, in situ X-ray reflectivity and X-ray absorption spectroscopy study, Thin Solid Films. 493 (2005) 67–76. https://doi.org/10.1016/j.tsf.2005.07.034.
[48] S. Choi, J. Kang, J. Park, Y.-C. Kang, Tin nitride thin films fabricated by reactive radio frequency magnetron sputtering at various nitrogen gas ratios, Thin Solid Films. 571 (2014) 84–89. https://doi.org/10.1016/j.tsf.2014.10.035.
[49] T.D. Veal, N. Feldberg, N.F. Quackenbush, W.M. Linhart, D.O. Scanlon, L.F.J. Piper, S.M. Durbin, Band Gap Dependence on Cation Disorder in ZnSnN2 Solar Absorber, Adv. Energy Mater. 5 (2015) n/a-n/a. https://doi.org/10.1002/aenm.201501462.

[50] J. Tauc, R. Grigorovici, A. Vancu, Optical Properties and Electronic Structure of Amorphous Germanium, Phys. Status Solidi B. 15 (1966) 627–637. https://doi.org/10.1002/pssb.19660150224.
[51] X. Duan, Y. Jiang, Annealing effects on the structural and electrical transport properties of n-type Bi2Te2.7Se0.3 thin films deposited by flash evaporation, Appl. Surf. Sci. 256 (2010) 7365–7370. https://doi.org/10.1016/j.apsusc.2010.05.069.
[52] A. K. Kulkarni, Kirk H. Schulz, T. S. Lim, M. Khan, Dependence of the sheet resistance of indium-tin-oxide thin films on grain size and grain orientation determined from X-ray diffraction techniques, Thin Solid Films 345 (1999) 273-277. https://doi.org/10.1016/S0040-6090(98)01430-8
[53] D. Stieler, V. L. Dalal, K. Muthukrishnan, M. Noack, E. Schares, Electron mobility in nanocrystalline silicon devices, J. Appl. Phys. 100 (2006) 036106. https://doi.org/10.1063/1.2234545
[54] A.N. Fioretti, A. Zakutayev, H. Moutinho, C. Melamed, J.D. Perkins, A.G. Norman, M. Al-Jassim, E.S. Toberer, A.C. Tamboli, Combinatorial insights into doping control and transport properties of zinc tin nitride, J. Mater. Chem. C. 3 (2015) 11017–11028. https://doi.org/10.1039/C5TC02663F.
[55] L. Lahourcade, N.C. Coronel, K.T. Delaney, S.K. Shukla, N.A. Spaldin, H.A. Atwater, Structural and Optoelectronic Characterization of RF Sputtered ZnSnN2, Adv. Mater. 25 (2013) 2562–2566. https://doi.org/10.1002/adma.201204718.
[56] N. Feldberg, J.D. Aldous, W.M. Linhart, L.J. Phillips, K. Durose, P.A. Stampe, R.J. Kennedy, D.O. Scanlon, G. Vardar, R.L.F. Iii, T.Y. Jen, R.S. Goldman, T.D. Veal, S.M. Durbin, Growth, disorder, and physical properties of ZnSnN2, Appl. Phys. Lett. 103 (2013) 042109. https://doi.org/10.1063/1.4816438.
[57] S. Lany, A.N. Fioretti, P.P. Zawadzki, L.T. Schelhas, E.S. Toberer, A. Zakutayev, A.C. Tamboli, Monte Carlo simulations of disorder in ZnSnN2 and the effects on the electronic structure, Phys. Rev. Mater. 1 (2017) 035401. https://doi.org/10.1103/PhysRevMaterials.1.035401.
[58] B. Traoré, G. Bouder, W. Lafargue-Dit-Hauret, X. Rocquefelte, C. Katan, F. Tran, M. Kepenekian, Efficient and accurate calculation of band gaps of halide perovskites with the Tran-Blaha modified Becke-Johnson potential, Phys. Rev. B. 99 (2019) 035139. https://doi.org/10.1103/PhysRevB.99.035139.

Table 1: Chemical composition of $MgSnN_2$ films prepared at different substrate temperatures

T_{sub} (°C)	N (at. %)	Mg (at. %)	Sn (at. %)	Mg/(Sn+Mg)
Room temperature	56.5	22.1	21.4	0.51
100	58.2	20.9	20.9	0.50
200	56.7	21.5	21.8	0.50
300	58.6	21.2	20.2	0.51
400	56.3	22.3	21.4	0.51
500	57.9	21.4	20.7	0.51

Table 2: Coherence lengthalong [001] of $ZnSnN_2$ thin films deposited with different substrate temperature, extracted from (002) peaks.

Substrate temperature (°C)	FWHM (002) (°)	Coherence length (nm)
Room temperature	0.300	29
100	0.235	38
200	0.216	42
300	0.207	44
400	0.196	47
500	0.184	51

Table 3: Hyperfine parameters of $MgSnN_2$ films (Isomeric Shift and Quadripolar Splitting).

Growth temperature (°C)	IS (mm/s)	QS (mm/s)
Room Temperature	1.058	0.937
100	1.069	0.938
200	1.063	0.930
300	1.063	0.920
400	1.057	0.910
500	1.049	0.905

Table 4: The optical band of as-deposited $MgSnN_2$ films. The uncertainty of the E_g value determination is ± 0.03 eV.

T_{sub}(°C)	E_g(eV)
Room temperature	2.27
100	2.28
200	2.29
300	2.28
400	2.38
500	2.43

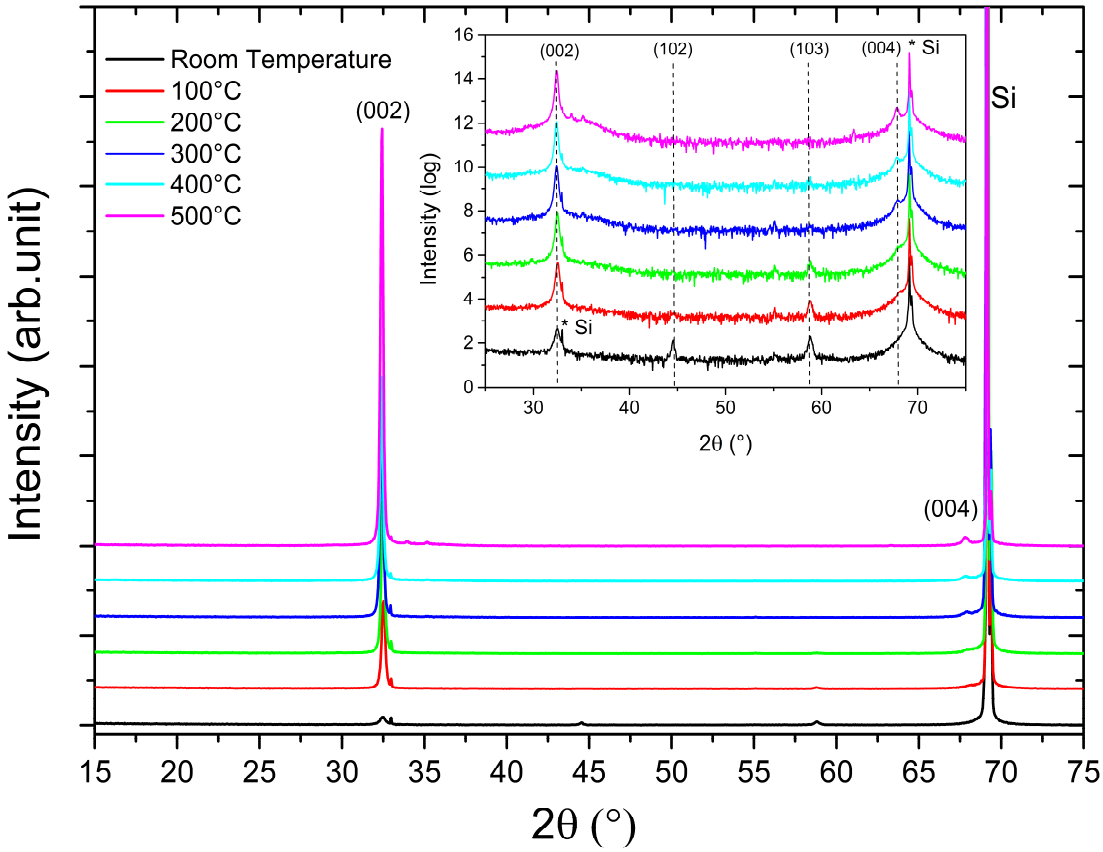

Figure 1: Specular XRD of $MgSnN_2$ thin films deposited at different substrate temperatures. The indexations correspond to the hexagonal structure type ($P6_3mc$). The inset corresponds to an enlargement of the X-ray diffractograms in the 25-75° range.

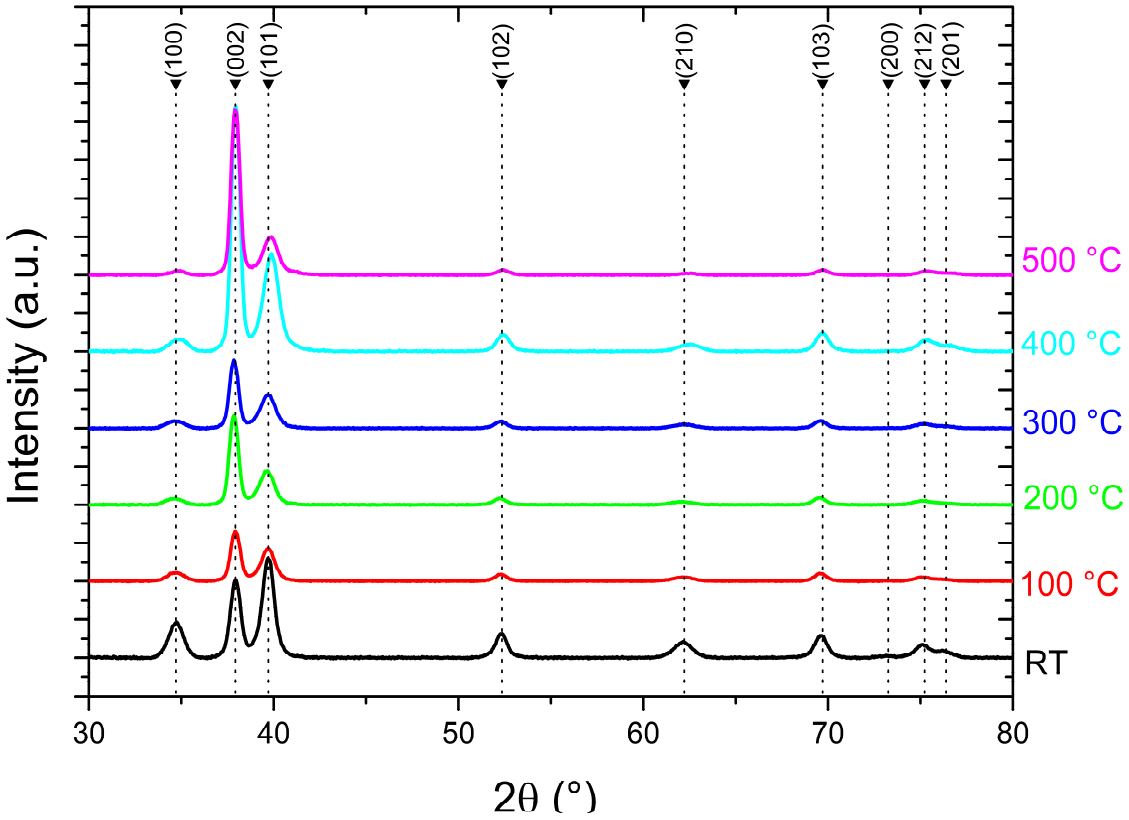

Figure 2: Cumulative X-ray diffractograms obtained at various χ angles for $MgSnN_2$ films deposited on fused silica substrates at different substrate temperatures. The indexations correspond to the hexagonal structure type ($P6_3mc$) with lattice parameters a = 3.459 and c = 5.507 Å.

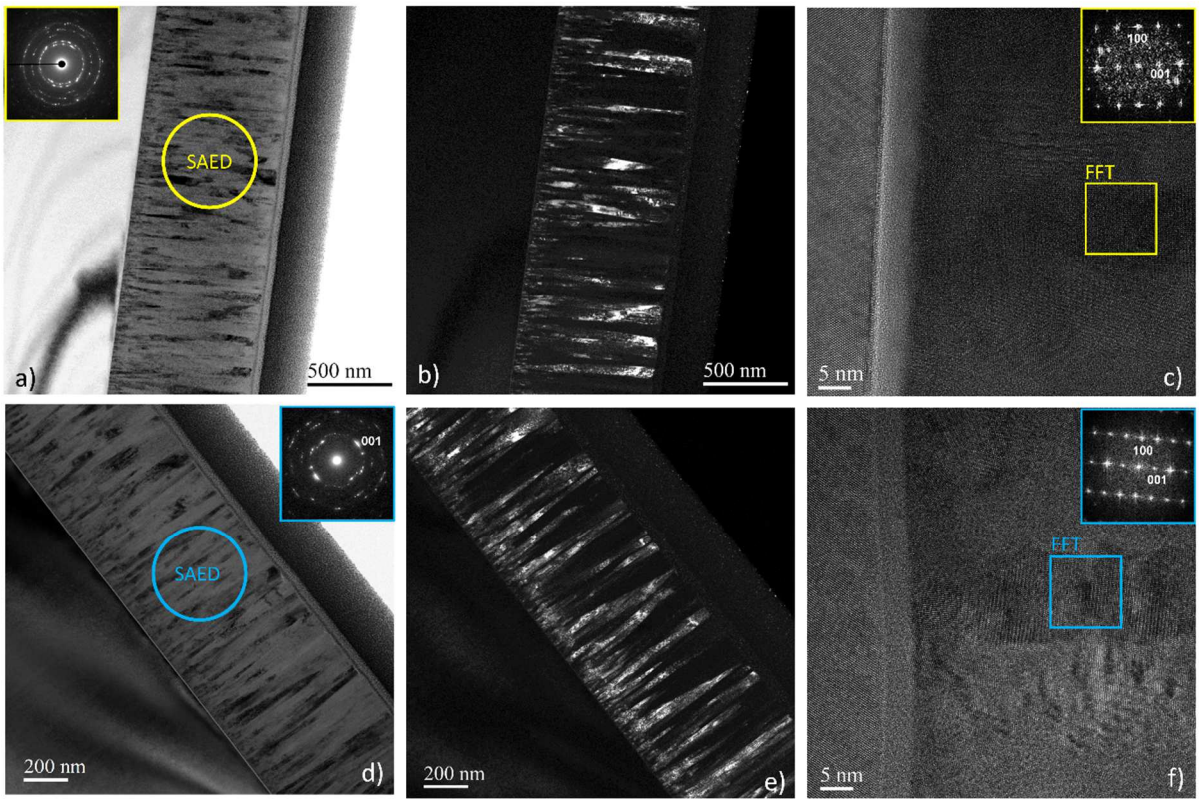

Figure 3: Bright field image and the inset shows selected area electron diffraction pattern (SAED) of $MgSnN_2$ films deposited at T_{sub}= room temperature (a) and at 500°C (d). Dark field image of $MgSnN_2$ films deposited at T_{sub}= room temperature (b) and at 500°C (e).HRTEM micrograph and corresponding FFT of $MgSnN_2$ thin films deposited at room temperature (c) and using T_{sub}= 500°C (f).

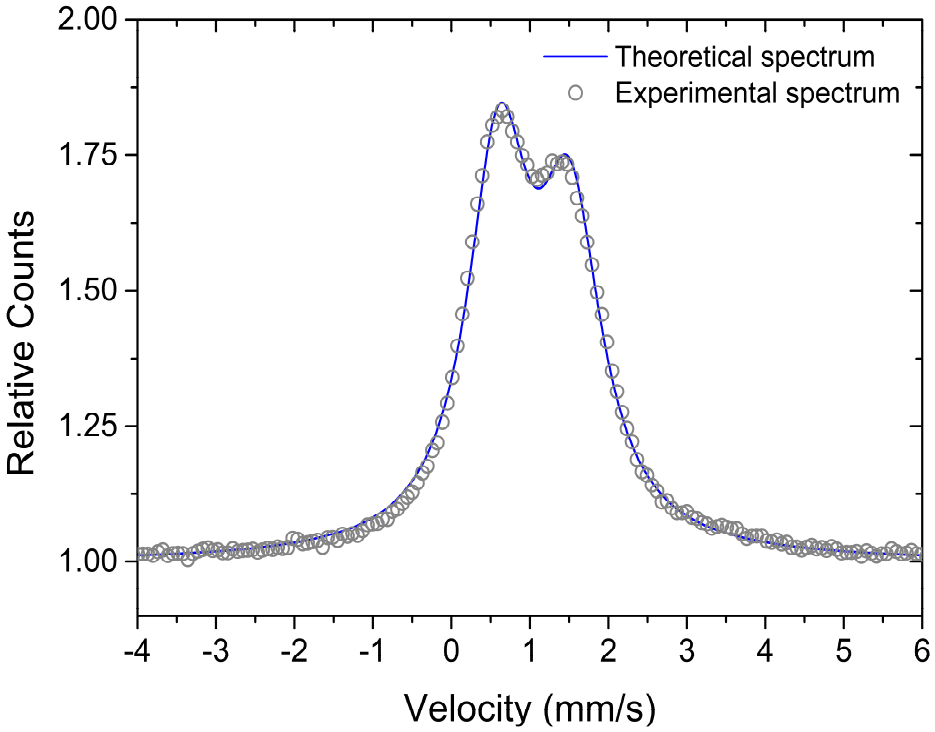

Figure 4: Experimental and simulated ^{119}Sn Mössbauer spectra of $MgSnN_2$.

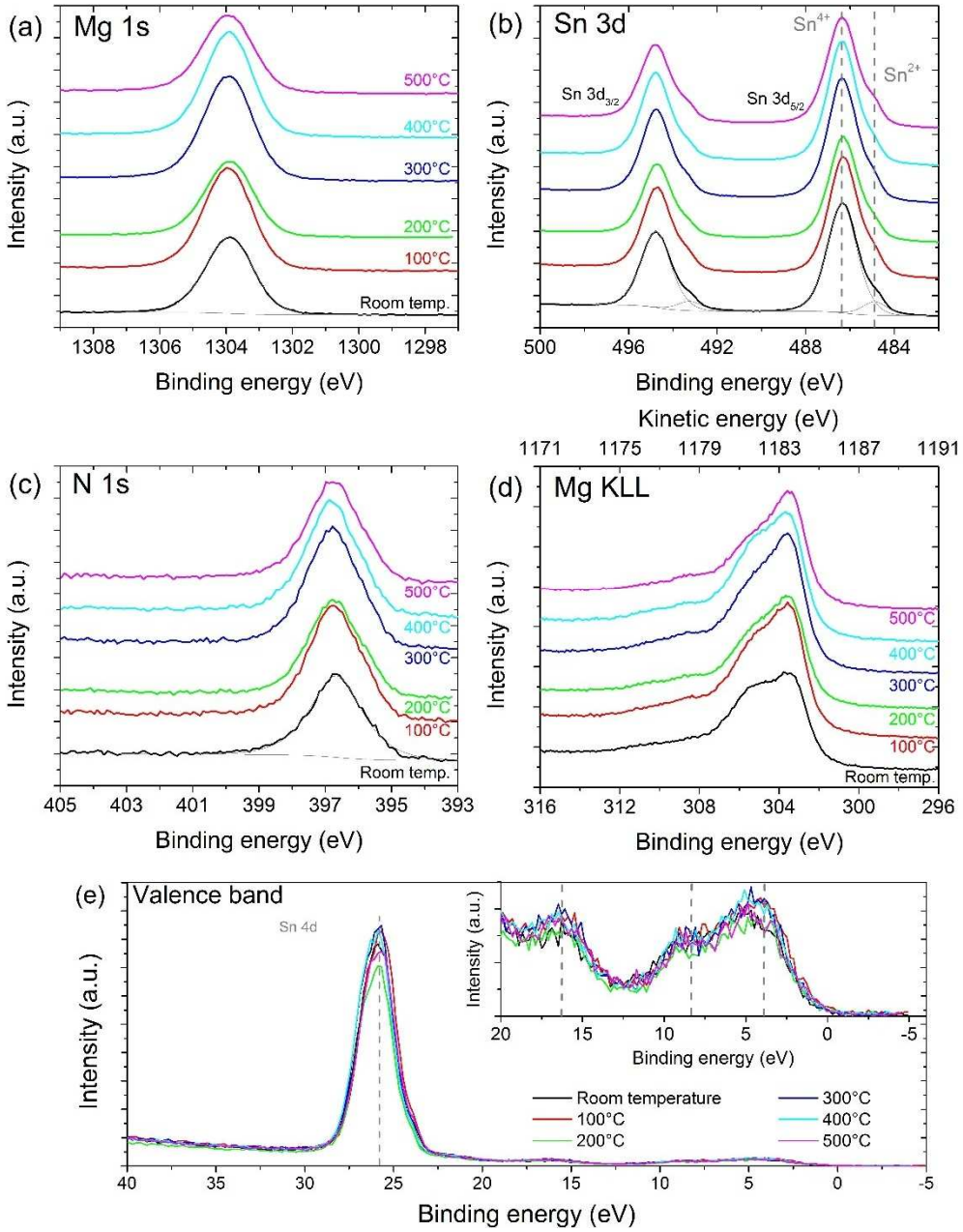

Figure 5: XPS analysis of $MgSnN_2$ films. High resolution spectra of (a) Mg 1s, (b) Sn 3d, (c) N 1s core levels, (d) Mg KLL Auger and (e) XPS valence band spectra of film deposited at different temperatures.

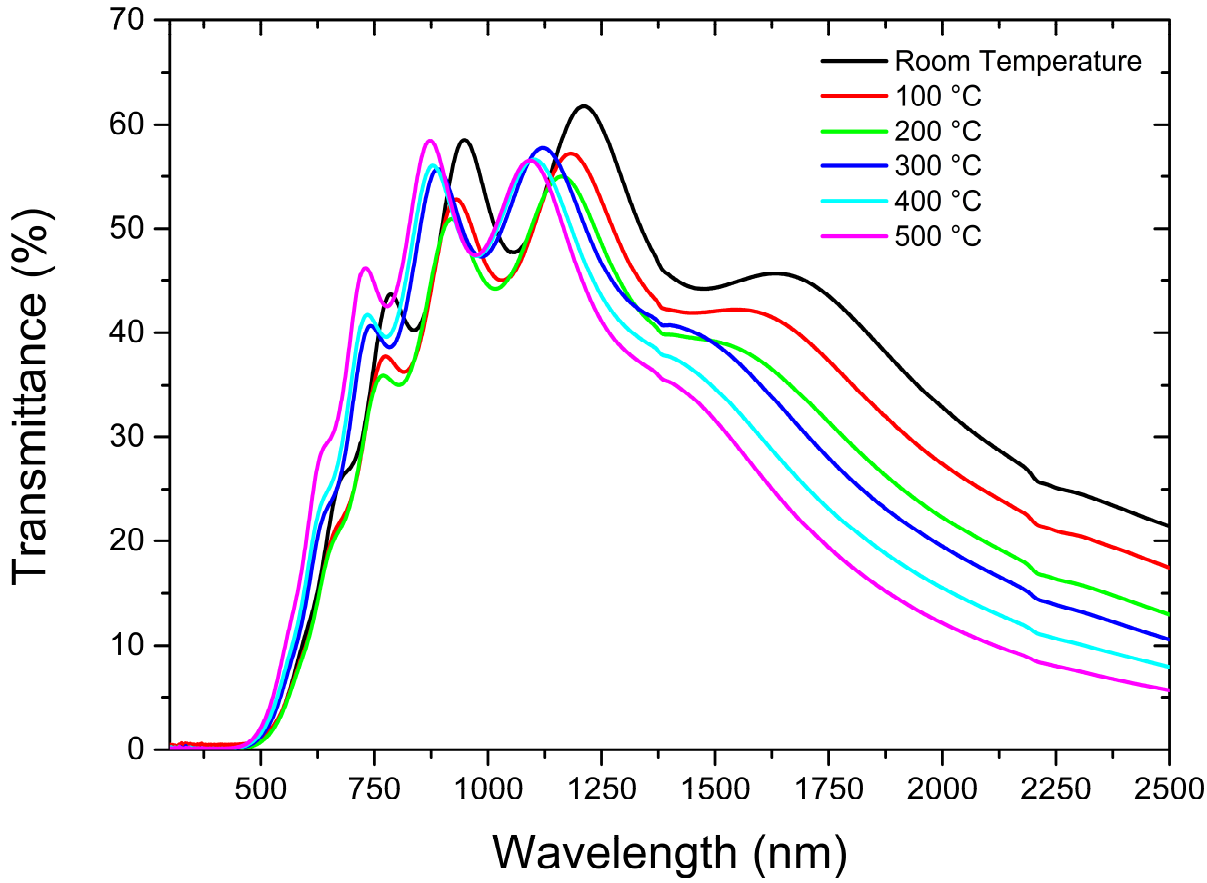

Figure 6: Transmittance of $MgSnN_2$ thin films grown at various deposition temperatures.

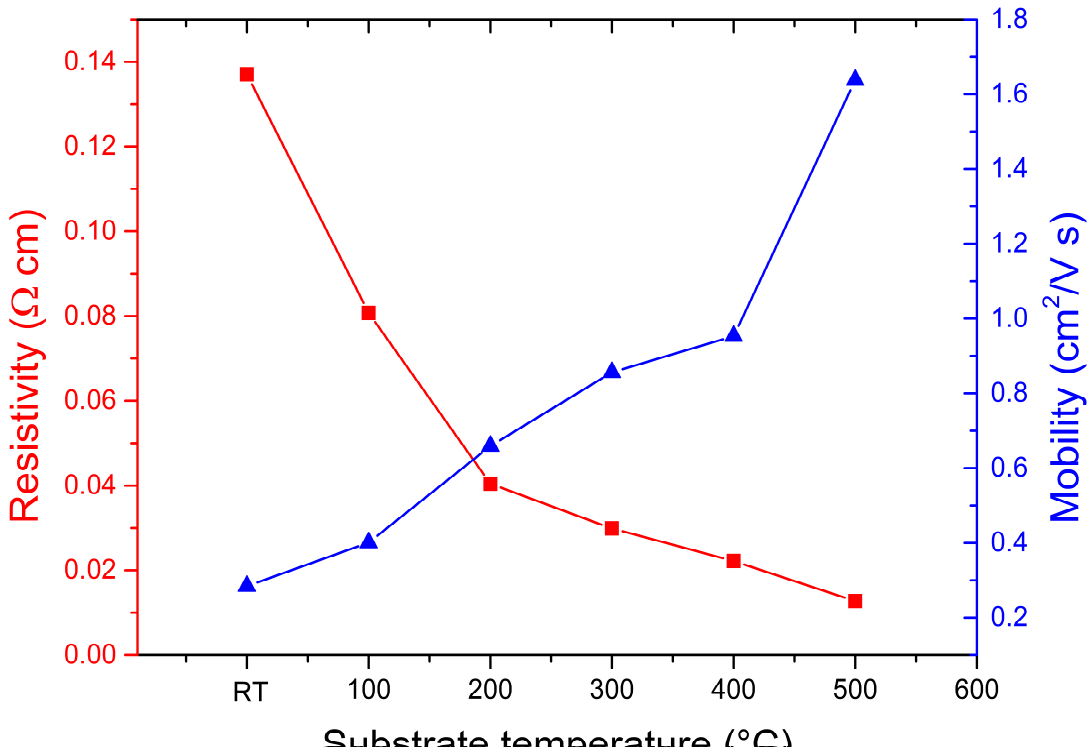

Figure 7: Evolution of the electrical resistivity (in red) and of the electron mobility (in blue) of $MgSnN_2$ thin films as function of deposition temperature

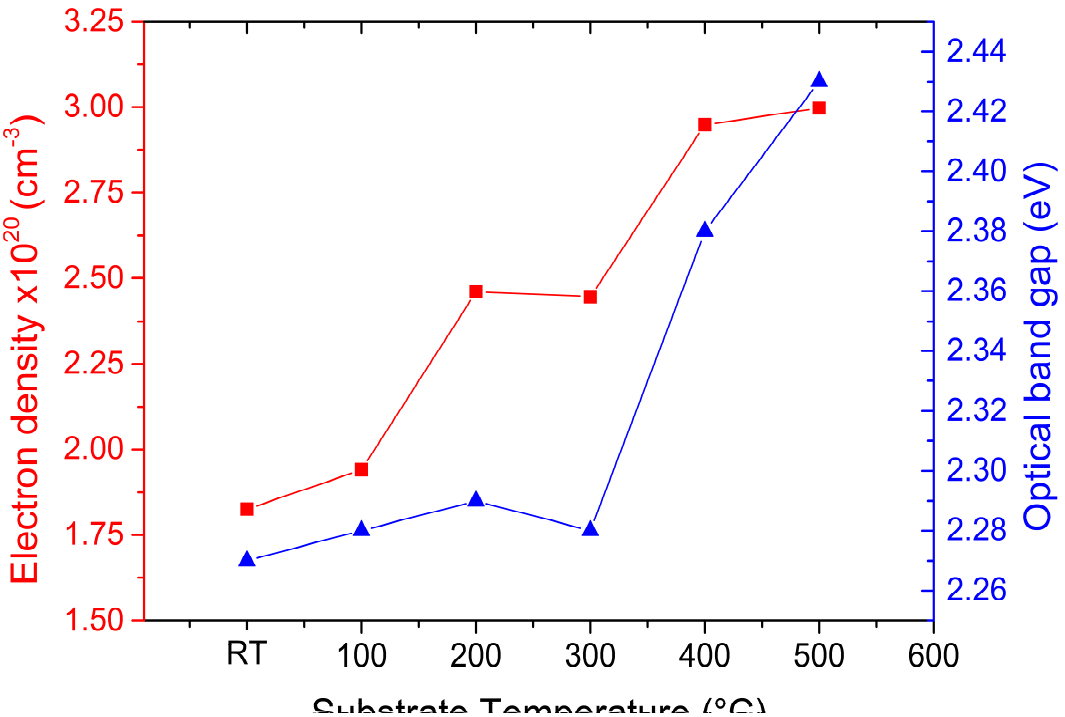

Figure 8: Influence of the deposition temperature on the electron density (in red) and the optical band gap of $MgSnN_2$ thin films.

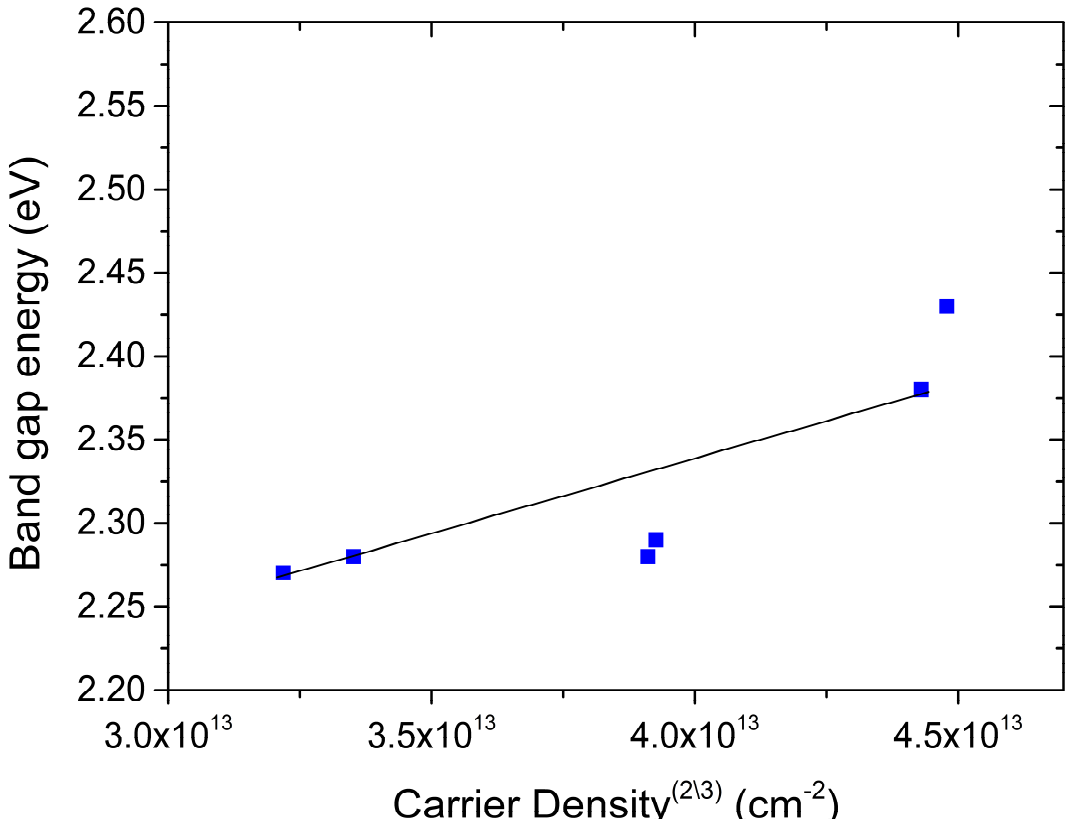

Figure 9: optical bandgap of $MgSnN_2$ thin films as function of the electron density to the power 2/3.

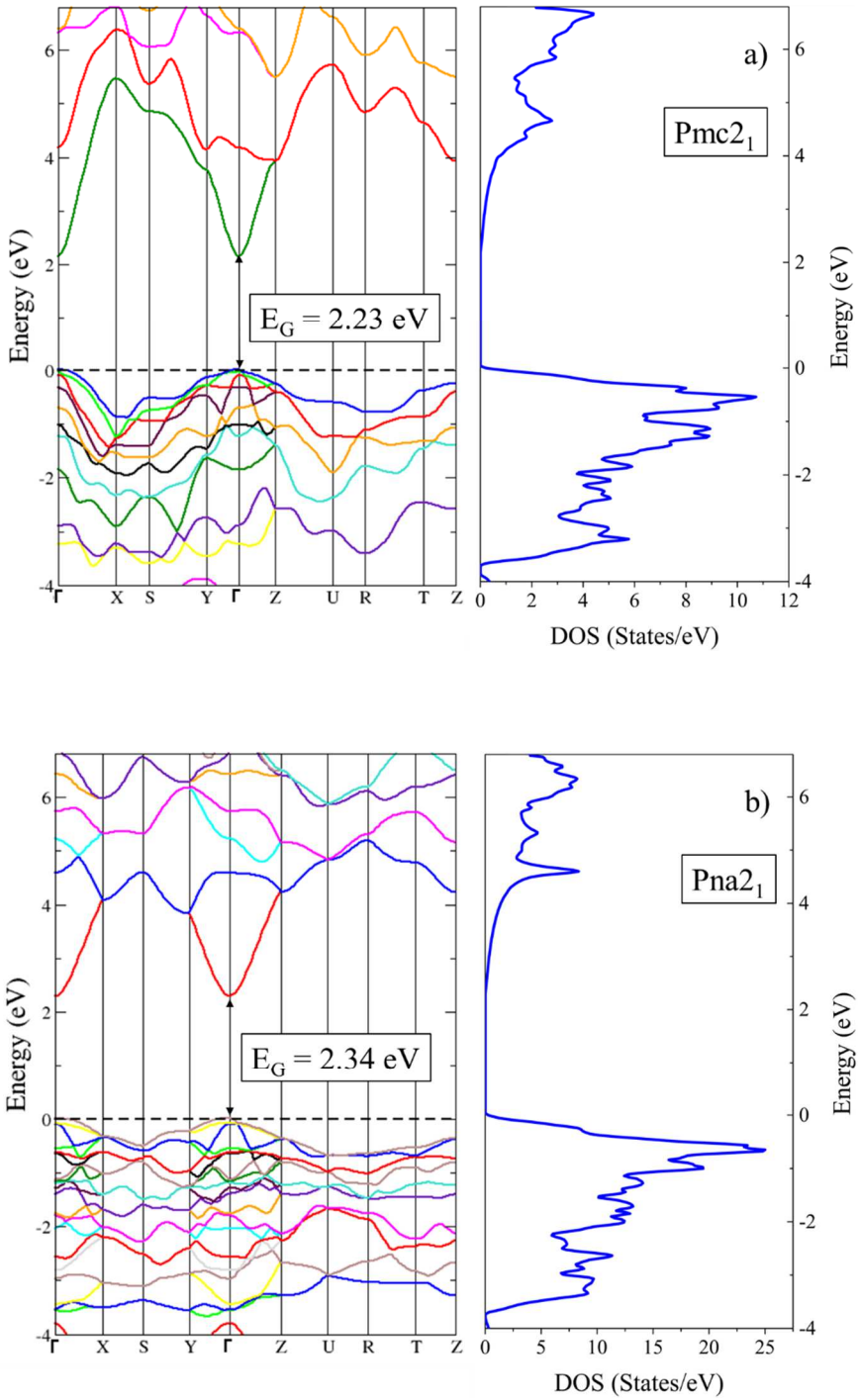

Figure 10: Electronic band structure with the corresponding band structure of $MgSnN_2$ for the two orthorhombic structures: a) $Pmc2_1$ and b) $Pna2_1$.

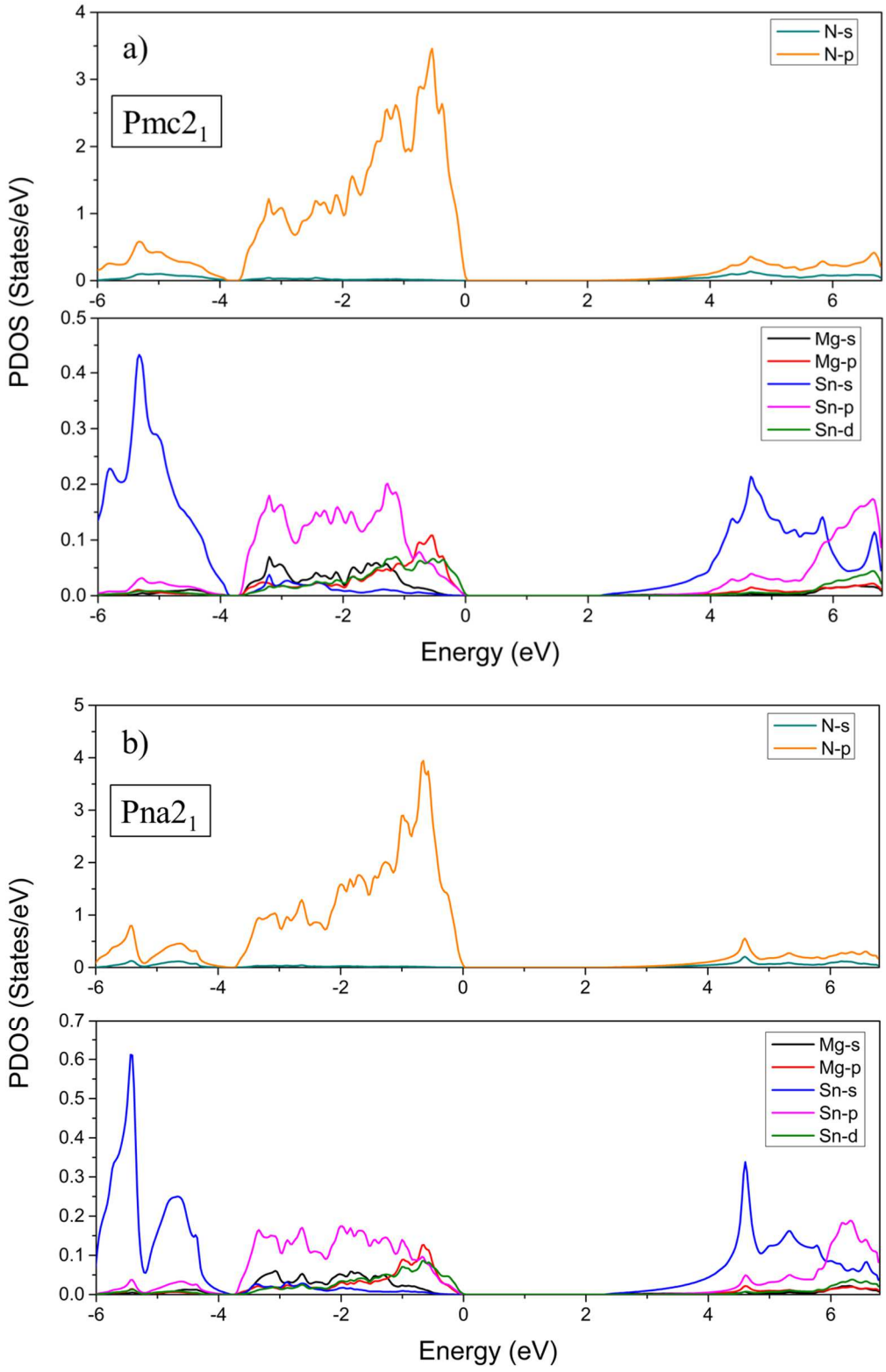

Figure 11: Projected density of states of $MgSnN_2$ in two different structures: a) $Pmc2_1$ and b) $Pna2_1$.

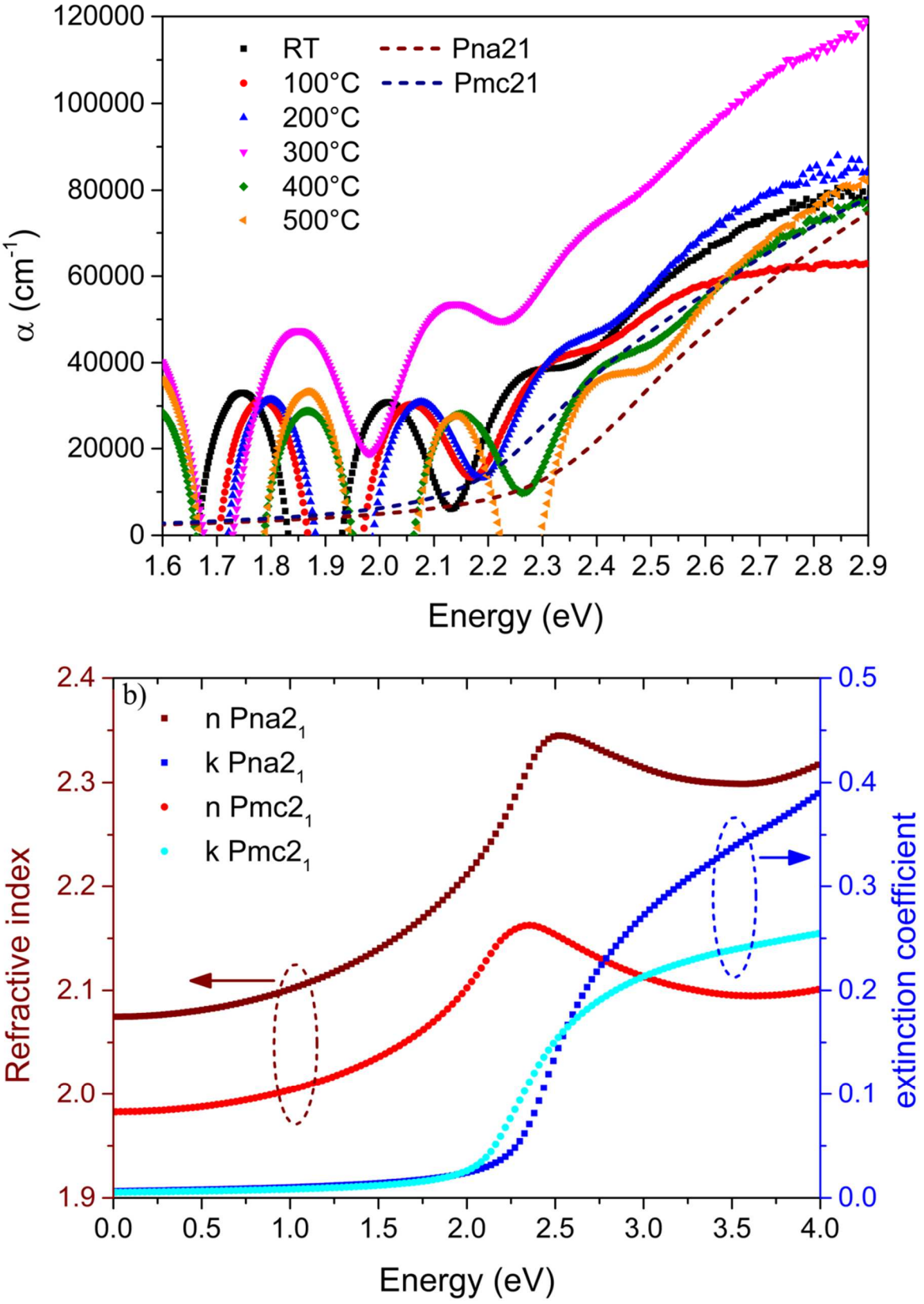

Figure 12: a) Comparison between experimental (at different temperatures) and calculated absorption coefficient for two orthorhombic space groups. b) Simulated refractive index and extinction coefficient for $MgSnN_2$ in $Pna2_1$ and $Pmc2_1$ space group.

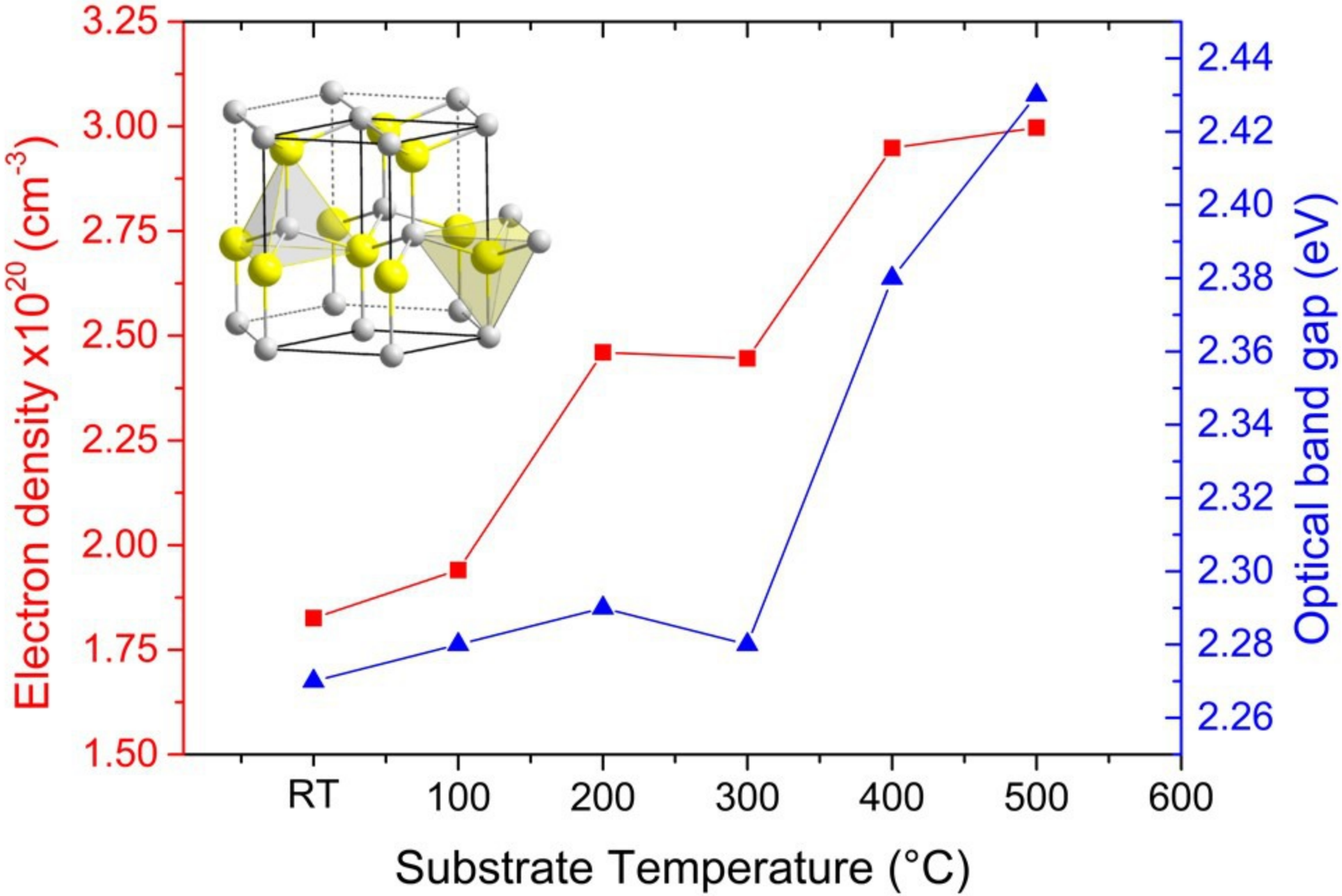
3.25
3.00
2.75
2.50
2.25
2.00
1.75
1.50
Electron density x10^20 (cm^-3)
2.44
2.42
2.40
2.38
2.36
2.34
2.32
2.30
2.28
2.26
Optical band gap (eV)
RT
100
200
300
400
500
600
Substrate Temperature (°C)